ADVANCED MATERIALS INTERFACES
Open Access
www.advmatinterfaces.de

Facile Tensile Testing Platform for In Situ Transmission Electron Microscopy of Nanomaterials

Bengisu Sari, Medha Dandu, Nathan Wood, Jacob Hochhalter, Amalya C. Johnson, Marca Doeff, Fang Liu, Archana Raja, Mary Scott, Rohan Dhall, and Roseanne Warren**

In situ tensile testing using transmission electron microscopy (TEM) is a powerful technique to probe structure-property relationships of materials at the atomic scale. In this work, a facile tensile testing platform for in situ characterization of materials inside a transmission electron microscope is demonstrated. The platform consists of: 1) a commercially available, flexible, electron-transparent substrate (e.g., TEM grid) integrated with a conventional tensile testing holder, and 2) a finite element simulation providing quantification of specimen-applied strain. The flexible substrate (carbon support film of the TEM grid) mitigates strain concentrations usually found in free-standing films and enables in situ straining experiments to be performed on materials that cannot undergo localized thinning or focused ion beam lift-out. The finite element simulation enables direct correlation of holder displacement with sample strain, providing upper and lower bounds of expected strain across the substrate. The tensile testing platform is validated for three disparate material systems: sputtered gold-palladium, few-layer transferred tungsten disulfide, and electrodeposited lithium, by measuring lattice strain from experimentally recorded electron diffraction data. The results show good agreement between experiment and simulation, providing confidence in the ability to transfer strain from holder to sample and relate TEM crystal structural observations with material mechanical properties.

1. Introduction

Establishing relationships between the mechanical properties of materials and their crystal structure is of paramount importance in understanding a material's response to mechanical deformation.[1] For most crystals, the application of mechanical strain is accompanied by the onset of plastic deformation through the formation and motion of crystal defects such as dislocations (slips) and twins. In the limit of high strains, these phenomena can lead to phase transitions, and ultimately, fracture.[2] Transmission electron microscopy (TEM) is unique in its ability to directly visualize the atomic structure of a material.[3] Hence, in situ mechanical deformation has been a subject of interest for electron microscopists since the early 1960s.[4,5] The principal aim of such work is the ability to quantitatively correlate applied mechanical strains with crystal structure imaging;the primary challenge lies in the difficultiesassociated with in situ sample preparation.

B. Sari, M. Dandu[+], A. Raja, M. Scott, R. Dhall
Molecular Foundry
Lawrence Berkeley National Laboratory
1 Cyclotron Rd, Berkeley, CA 94720, USA
E-mail: rdhall@lbl.gov

B. Sari, M. Scott
Department of Materials Science and Engineering
University of California
Berkeley, CA 94720, USA

N. Wood, J. Hochhalter, R. Warren
Department of Mechanical Engineering
University of Utah
Salt Lake City, UT 84112, USA
E-mail: roseanne.warren@utah.edu

A. C. Johnson
Department of Materials Science and Engineering
Stanford University
Stanford, CA 94305, USA

M. Doeff
Energy Storage and Distributed Resources Division
Lawrence Berkeley National Laboratory
Berkeley, CA 94720, USA

F. Liu
Department of Chemistry
Stanford University
Stanford, CA 94305, USA

A. Raja
Kavli Energy NanoScience Institute
University of California Berkeley
Berkeley, CA 94720, USA

The ORCID identification number(s) for the author(s) of this article can be found under https://doi.org/10.1002/admi.202400750

[+]Present address: Chemistry and Physics of Materials Unit (CPMU), Jawaharlal Nehru Centre for Advanced Scientific Research, Jakkur P.O., Bengaluru 560064, India

DOI: 10.1002/admi.202400750

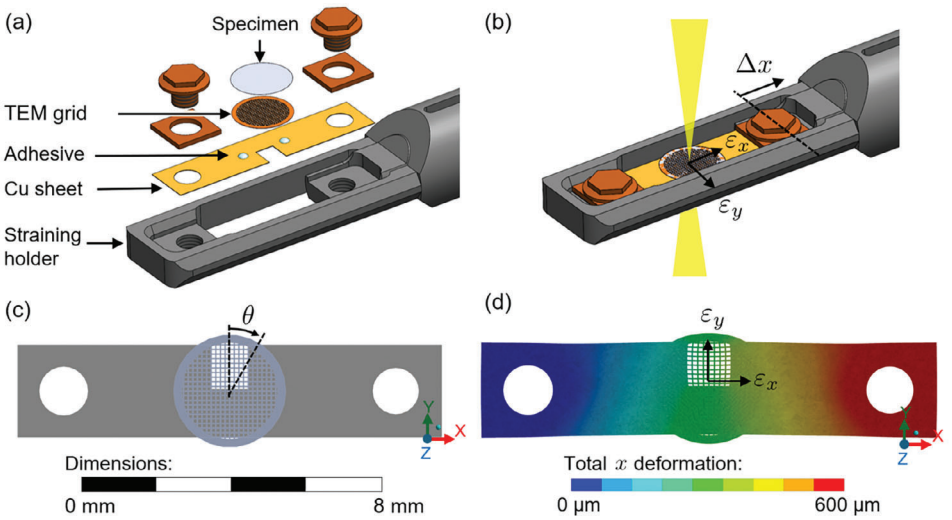

Figure 1. Tensile testing platform for in situ TEM including physical platform (a, b) and finite element simulation (c, d). a) Exploded view of the physical platform, which consists of a straining holder (Gatan 654), copper sheet, adhesive, TEM grid, and specimen. b) Assembly and in situ imaging with the physical platform. Uniaxial displacement of the copper sheet by the straining holder (Δx) produces x and y crystal strains (ε_x, ε_y) in the specimen. c) FEA simulation geometry including copper sheet and TEM grid oriented at angle θ relative to the copper sheet. d) Uniaxial displacements up to 600 µm are represented in the simulations.

In situ approaches that enable precise control and quantification of strain typically require complex, material-restrictive, sample preparation protocols. Various approaches have been adopted to fabricate thin specimens suitable for in situ mechanical deformation,[6–14] most prominent among them being focused ion beam (FIB) lift-out. Electron transparent FIB samples are suspended across an ≈2 µm wide gap in a pre-fabricated silicon chip, clamped on either side using ion beam deposition of platinum, and then stretched using a micro-electro-mechanical systems (MEMS)-based tensile testing stage.[15–17] The advantage of MEMS-based methods is a precise measure of true stresses and strains made possible by integrated force transducers, from which elastic stiffness constants, i.e., the bulk and shear modulus, can be obtained. This, however, comes at the cost of experimental complexity and challenges in sample preparation.

The alternative approach requires the use of samples that can be first machined into a dog-bone geometry and then thinned locally to electron transparency. The specimen is then clamped on both sides and elongated at typical rates of ≈2 µm s^{-1} using a finely geared DC motor. The specimens themselves are easy to prepare, and the experimental approach is easier to implement and less prone to failure than MEMS-based approaches. Innovations using a linear motion actuator (i.e. coupler pin) and cartridge-type blade design have enabled in situ straining holders that accommodate high tilt angles for 3D electron tomography,[18] in conjunction with large tensile[19] and shear strains.[20] Unfortunately, thinning-based sample preparation approaches limit researchers to material systems such as metals that can be machined via conventional methods and thinned via ion-milling,[21–25] or thin polymer samples that can be prepared by ultramicrotomy.[19,20] Presently lacking is an approach that provides a facile and flexible sample preparation methodology while also providing some value of expected strain in the specimen under tension.

Prior work has demonstrated the ability to perform tensile tests of thin films deposited on a flexible substrate such as polyimide,[26] or polydimethylsiloxane.[27–29] Besides simply enabling the straining of thin films, the flexible substrate offers another key benefit, which is the suppression of strain localization observed in free-standing thin films. Local strain fluctuations are exacerbated in free-standing films as they are accompanied by "necking", which reduces the local cross-sectional area of the film, thus concentrating stress. When a thin film adheres to a flexible substrate, the strain is delocalized across the specimen, which has allowed metal films to be stretched by as much as 50% under tensile load.[30,31] While such approaches support a wide range of sample preparation strategies for in situ deformation under large strains, the ability to accurately quantify the applied load is lost.

In this work, we couple for the first time a facile sample preparation approach based on thin film deposition or transfer to a commercially-available carbon-coated TEM grid with finite element modeling enabling precise determination of strain profiles under elongation. (**Figure 1**). The specimen is deposited on an ultra-thin, flexible, electron-transparent substrate (carbon support film of the TEM grid), which is then affixed to a macroscopic tensile testing platform machined out of a 25 µm thick copper sheet (2.5 mm × 11 mm) (Figure 1a). The copper platform is loaded into a Gatan 654 straining holder, clamped on either end with screws, and elongated using a finely geared DC motor while imaging (Figure 1b). The sample preparation process is almost identical to what is used for conventional TEM sample preparation, and thin films can be spin-coated, sputter-coated, electrodeposited, or transferred to the flexible substrate

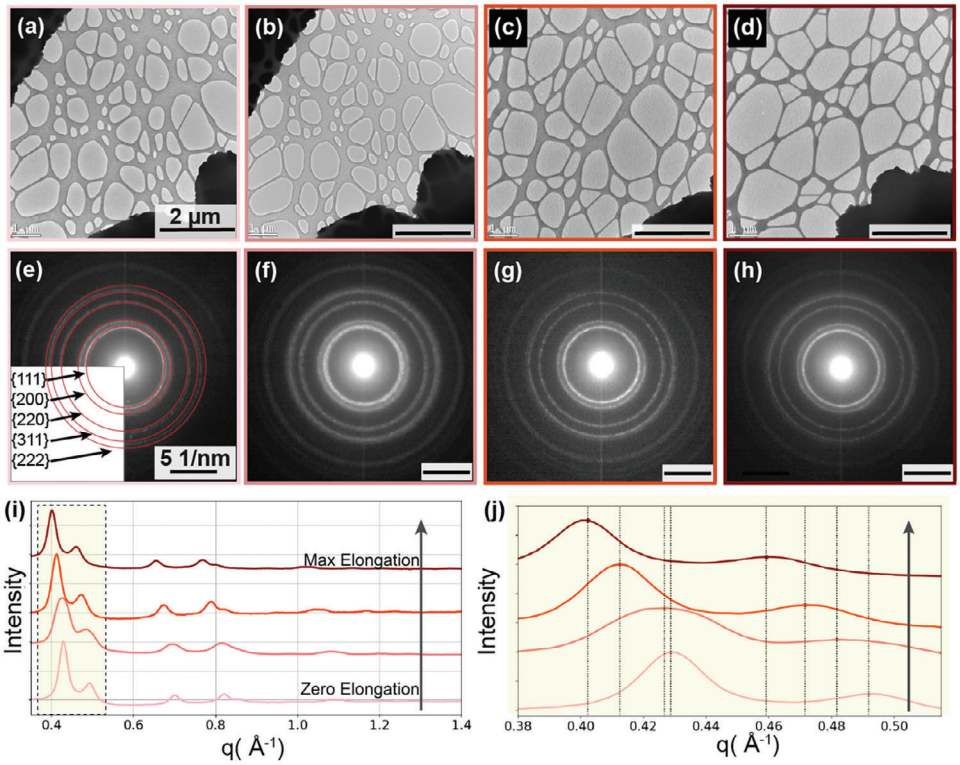

Figure 2. Strain analysis of sputtered Au–Pd. a–d) Bright-field images under increasing elongation of the tensile testing platform (left to right). e–h) SAED patterns of the corresponding regions shown in (a–d). i) Radial profiles of the corresponding SAED patterns in (e–h). j) Zoomed-in radial profiles around the dashed rectangle depicted in (i). The direction of the arrows in (i) and (j) corresponds to increasing elongation of the tensile testing platform. The direction of elongation of the TEM specimen is aligned with the vertical direction in the TEM images, and there is a rotational offset of ≈5° between the images and the diffraction patterns.

via wet transfer. Finite element analysis (FEA) simulations allow us to calculate the expected strain in our samples for varying TEM grid bar geometries and materials (Figure 1c,d). At the same time, analysis of electron diffraction patterns under mechanical tension allows us to directly measure the crystal strain in the thin films. We find that the experimentally measured strain values are in good agreement with our simulations. Additionally, our model sheds light on strain non-uniformities expected for this geometry. Due to the biaxial nature of the TEM grid bars relative to the straining holder displacement, the distribution of stress and strain across the field of view is necessarily non-uniform. Through finite element modeling, we are able to quantify the distribution of strain across the specimen for any grid bar geometry, thus ensuring repeatability and reproducibility, as well as consistencies in data analysis and interpretation, despite the variation in strain field. We estimate reasonable confidence intervals for the expected values of strain through our finite element models. We demonstrate the flexibility of this approach by performing straining experiments on three disparate material systems prepared with three different techniques: 1) a sputter-coated polycrystalline film of Au–Pd, 2) few-layer transferred WS_2, and 3) electrodeposited Li. We expect that such analysis will improve the reliability and reproducibility of TEM observations under mechanical strain, and help create standards in the field of in situ tensile testing.

2. Results and Discussion

2.1. Sputter-Coated Au–Pd

Figure 2 shows the results of our first experimental dataset, which is acquired on a sputter-coated film of Au–Pd with a thickness of ≈10 nm. TEM studies are important for understanding the nucleation and atomic crystallization mechanisms of metal thin films.[32,33] The ability to directly deposit such films onto a tensile testing platform without additional thinning or transfer procedures enables the study of process-structure-property relationships for these materials. Figure 2a–d shows a sequence of bright-field TEM images of the Au–Pd specimen at increasing elongations of the tensile testing platform. The deposited film is a finely-grained polycrystalline thin film, and hence the contrast in these images arises from the morphological fluctuations in the underlying carbon support. The large particle in the bottom right is likely dust contamination, which was used to track the region of interest. The TEM grid and specimen experience dimensional changes along horizontal and vertical grid bar orientations that are approximately linear with straining holder uniaxial displacement (Figure S5, Supporting Information). The exact dimensional change of the grid and specimen will depend on the orientation of the grid relative to the copper sheet, as explored further in the FEA simulation section below, and the

applied strain may be more or less biaxial in nature depending on the location of the region of interest relative to the copper mesh. Figure 2e–h provides the corresponding selected area electron diffraction (SAED) patterns of the Au–Pd specimen using a selected area aperture of 1 µm diameter when back-projected to the specimen plane. The SAED patterns show circular diffraction rings originating from different atomic planes of the FCC crystal of Au–Pd. The best-fit ellipse that passes through each of the rings (overlaid in red dashed lines) is determined for each polycrystalline diffraction ring using numerical routines in the py4DSTEM software package.[34] The center of these curves is used as the center of the diffraction pattern. This allows us to azimuthally integrate the observed diffraction data, yielding an integrated diffraction intensity as a function of the radial distance, q, away from the center of the diffraction pattern (in $Å^{-1}$). This radial distance corresponds to the magnitude of the scattering vector i.e., $|\vec{q}|$, in reciprocal space. These curves are shown in Figure 2i, where peaks corresponding to diffraction from the {111}, {200}, and {220} planes are observed. Figure 2j zooms in on the lowest-order diffraction peaks, corresponding to the {111} and {200} lattice spacings. The vertical dashed lines denote the peak positions which are obtained by fitting with Gaussian functions. The arrows in Figure 2i,j indicate increasing elongation of the tensile testing platform, which corresponds to increasing values of strain. As seen in these plots, elongation of the tensile testing platform is accompanied by a reduction in the reciprocal space lattice vector, i.e., an increase of the real space lattice constants. In our strain analysis, we compare the SAED patterns under increasing elongations to a reference pattern acquired before sample elongation, thereby establishing a relative measurement that eliminates the need for precise distortion calibrations resulting from variations in the TEM projector lenses. We are unable to measure any anisotropy induced in the polycrystalline films as a result of elongation, which may be a result of the limited precision with which we can detect Bragg reflections, or possibly a consequence of the strain accommodation at grain boundaries.

2.2. 2D Single Crystalline WS_2

Figure 3 provides the results of our second experimental dataset, acquired on a few-layer transition metal dichalcogenide (TMDC) semiconductor, WS_2. In the case of laterally small, exfoliated flakes of 2D materials, imaging and nanomechanical testing using TEM is conventionally done by stamping the flakes onto the substrate. Stamping methods typically have low yields of transfer and adhesion. In contrast, the facile tensile testing platform method demonstrated here offers a convenient way of scooping the flakes onto commercially-available grids and stretching them. Figure 3a–e shows bright-field TEM images of the specimen under elongation. Significant diffraction contrast arising from bending of the WS_2 film is evident in Figure 3a–c. As the sample is elongated, the flattening of the WS_2 eliminates this diffraction contrast (Figure 3d,e), indicating that the sample is indeed in tension. We collect SAED patterns at ten different elongations, of which five are shown in Figure 3f–j. Figure 3k shows the azimuthally integrated diffraction intensities of all the collected SAED patterns, where the arrow indicates increasing elongation of the tensile testing platform. Figure 3l,m highlights the dominant peaks, originating from diffraction from the {1 0 −1 0}, {2 −1 −1 0}, and {2 0 −2 0} lattice planes in the hexagonal structure of WS_2. We observe a shift in the peaks of radial diffraction intensity with increasing elongation, indicating a reduction in the size of the reciprocal lattice due to an expansion of the real space crystal lattice.

Using numerical routines in the py4DSTEM package, we identify the positions of Bragg reflections in SAED patterns with sub-pixel accuracy. From these positions, we derive two distinct non-collinear 2D reciprocal space basis vectors as illustrated in Figure 3f, corresponding to the [$\bar{1}$010] and [01$\bar{1}$0] directions. As the specimen is strained, these basis vectors undergo a distortion which can be represented by a matrix transformation (D) given by Equation (1):

$$D = (G_0 * G^{-1})^t \tag{1}$$

where G_0 and G represent the undistorted and strained basis vectors, respectively, of the form $\begin{pmatrix} g_{x1} & g_{x2} \\ g_{y1} & g_{y2} \end{pmatrix}$. Following the formalism presented by Cooper,[35,36] this distortion matrix can be further separated into two components: a rotation matrix (R), and a pure deformation matrix (F). In the approximation of small strains, the rotation matrix is linked to the antisymmetric part of D:

$$R = I + \frac{1}{2}(D - D^t) \tag{2}$$

and the strain, E, is linked to the symmetric part of D:

$$E = \frac{1}{2}(D^t + D) - I \tag{3}$$

where I represents the identity matrix. This enables us to extract four physically meaningful components from the distortion matrix D encompassing three in-plane strain components, ε_x, ε_y, ε_{xy}, along with a rotation angle θ. These components are plotted in Figure 3n–q as a function of increasing specimen elongation.

In contrast to the polycrystalline film of Au–Pd, we see evidence for anisotropic strain in this single crystalline film. As shown in Figure 3n,o, the lattice undergoes expansion along the x-direction, and contraction along the y-direction. We note that the direction of elongation does not perfectly align with the crystal lattice x-direction. This anisotropy is particularly apparent in hexagonal TMDC structures, where it has been shown by theoretical calculations that an ultra-large elastic strain close to 20% along the armchair direction and 15% along the zigzag direction can be achieved in ideal single crystalline monolayer WS_2.[37] We are unable to reach these large values of strain, most likely due to slipping of the TMDC flakes over the amorphous carbon substrate under elongation. Several methods are available to promote specimen adhesion and reduce slippage under strain, including: post-baking, plasma cleaning, selective metal deposition clamping,[38] custom microfabricated adhesion-enhanced grids,[39] and polymer encapsulation.[40] Quantification and optimization of slippage reduction methods with the tensile testing platform is planned for future work.

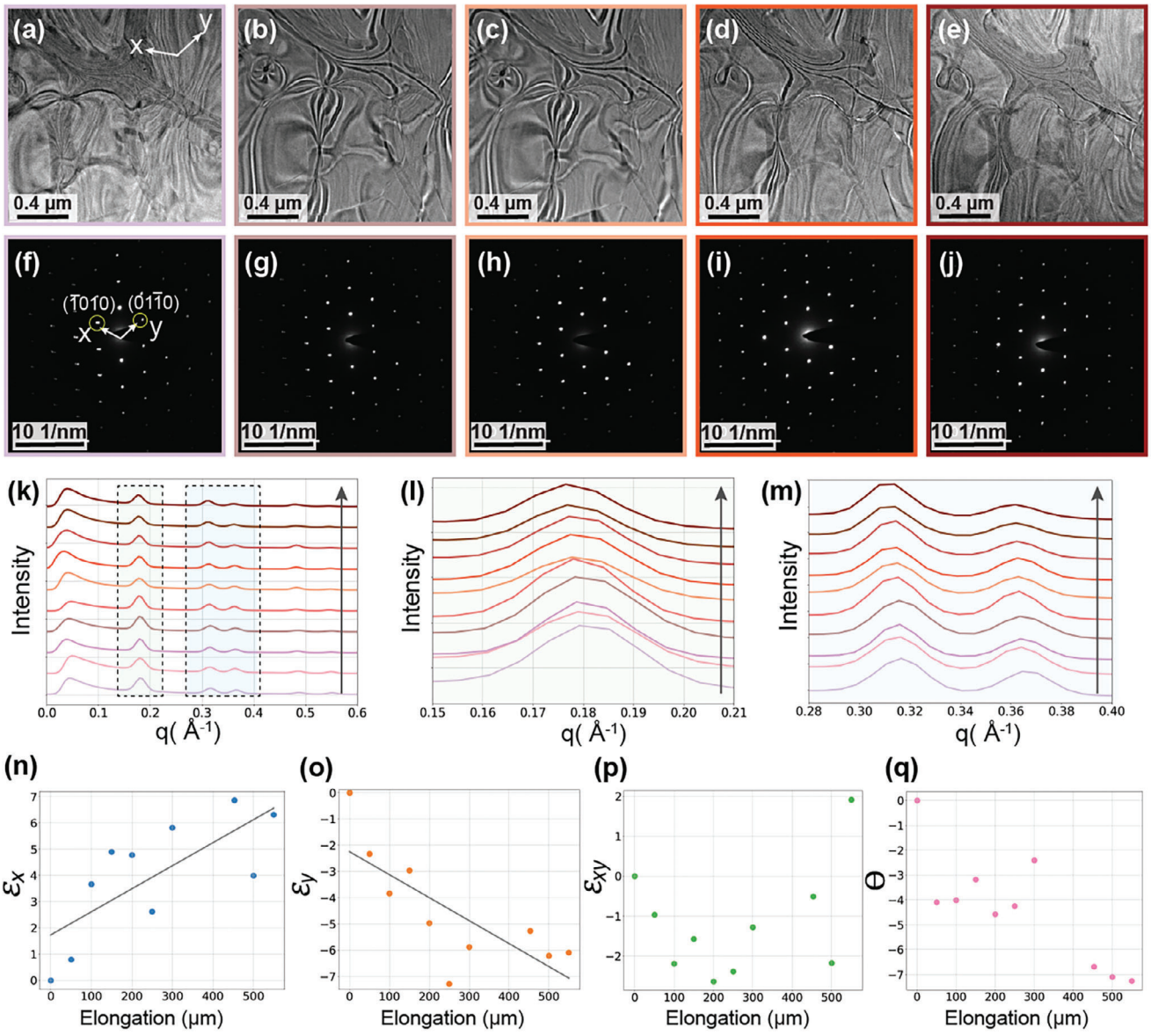

Figure 3. Strain analysis of few-layer WS_2. a–e). Bright-field images under increasing elongation (left to right). f–j) SAED patterns corresponding to the areas in (a-e). k) Radial profiles of diffraction intensity from SAED patterns. l-m) Zoomed-in radial profiles of diffraction intensity from SAED patterns around the regions highlighted in (k). Arrows represent the direction of increasing elongation. n-q) The extracted in-plane crystal strain components ε_x, ε_y, ε_{xy}, and a rotation angle θ from analysis of SAED patterns. "Elongation" refers to straining holder displacement (*i.e.* Δx in Figure 1b).

2.3. Electrodeposited Li

Figure 4 provides a final demonstration of a sample preparation technique that can be employed with our tensile testing platform: direct electrodeposition of Li metal onto a TEM grid. FIB lift-out of electron beam-transparent Li samples is notoriously difficult and must be performed under cryogenic conditions.[41] Direct electrodeposition of Li metal onto TEM grids is an effective approach for preparing Li thin films for electron beam imaging.[42] Due to the lack of air-free transfer from the glovebox to microscope, the imaged sample in Figure 4 presents as Li_2O, however, the utility of the approach is clearly demonstrated. Figure 4a provides a bright-field TEM image of the electrodeposited Li sample, along with the indexed electron diffraction pattern (Figure 4b). Figure 4c shows the azimuthally integrated profiles of the diffraction patterns under an applied mechanical strain. Figure 4d zooms in on the {002} peak.

Due to the challenging nature of electrodeposited Li sample preparation, we find the TEM grids are often damaged, as seen in Figure 4a. Figure 4d results, measured on an undamaged grid square, show that upon elongation, the thin film in this square exhibits a similar contraction of the reciprocal space lattice as observed in polycrystalline Au–Pd films. However, under strain, we observe the emergence of cracks in the thin film (Figure 4a) which ultimately release the strain in the thin film, and the observed lattice constants relax back to their

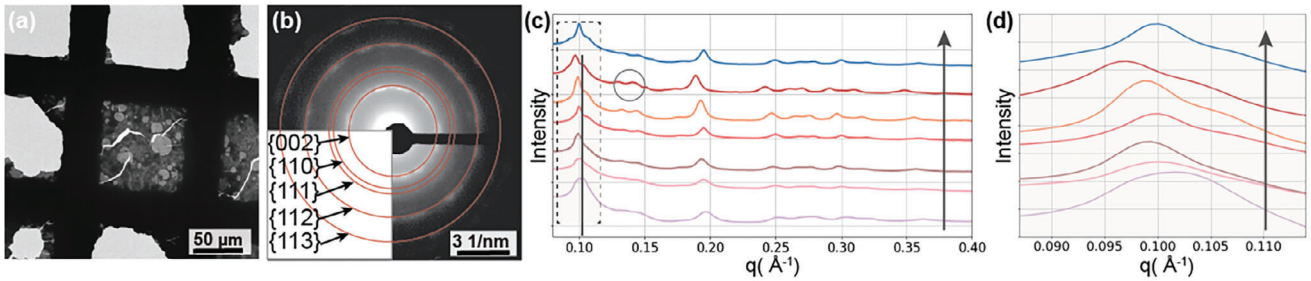

Figure 4. Strain analysis of Li_2O. a) Bright-field image of oxidized Li metal deposited on a TEM grid. b) SAED pattern of polycrystalline Li_2O. c,d) Radial profiles of Li_2O diffraction patterns under increasing strain. Arrows represent the direction of increasing elongation.

original state (blue curve in Figure 4d). With careful control of air exposure conditions and improved grid handling protocols, we expect that the electrodeposited sample preparation method demonstrated here could be extended to in situ tensile testing of Li metal films in future work. Such work is of considerable importance in understanding the mechanisms of dendrite formation and failure in all solid-state lithium metal batteries.[43]

2.4. FEA Simulation

Figure 5 provides results of tensile platform FEA simulations and a comparison of simulated versus experimental strains. The simulated normal engineering strain ε_x of the entire tensile testing platform (copper sheet and TEM grid) is shown in Figure 5a. Normal engineering strains vary from ≈–0.2% to 22% for a straining holder displacement of 600 µm. The specified area within Figure 5a is the viewing window cut-out where our strains of interest occur. This is also the region with the highest strain. Figure 5b shows a magnified image of this area, where strain variations in *x*- and *y*-directions can be observed both across the viewing window cut-out and within individual grid squares. In Figure 5b, a specific grid square is identified where experimental imaging of WS_2 was performed; this grid square is further magnified in Figure 5c. Because the model simulates TEM grid bars only and neglects ultrathin layers (carbon support film and thin-film specimen) within the grid squares, the contour plot in Figure 5c is limited to strains around the outside of the square. The ultrathin layers were neglected assuming they do not change the effective elastic modulus given their negligible volume and stiffness compared to the grid. This assumption was justified using the rule of mixtures (see Supporting Information). Linear interpolation and engineering-to-true strain conversion was used

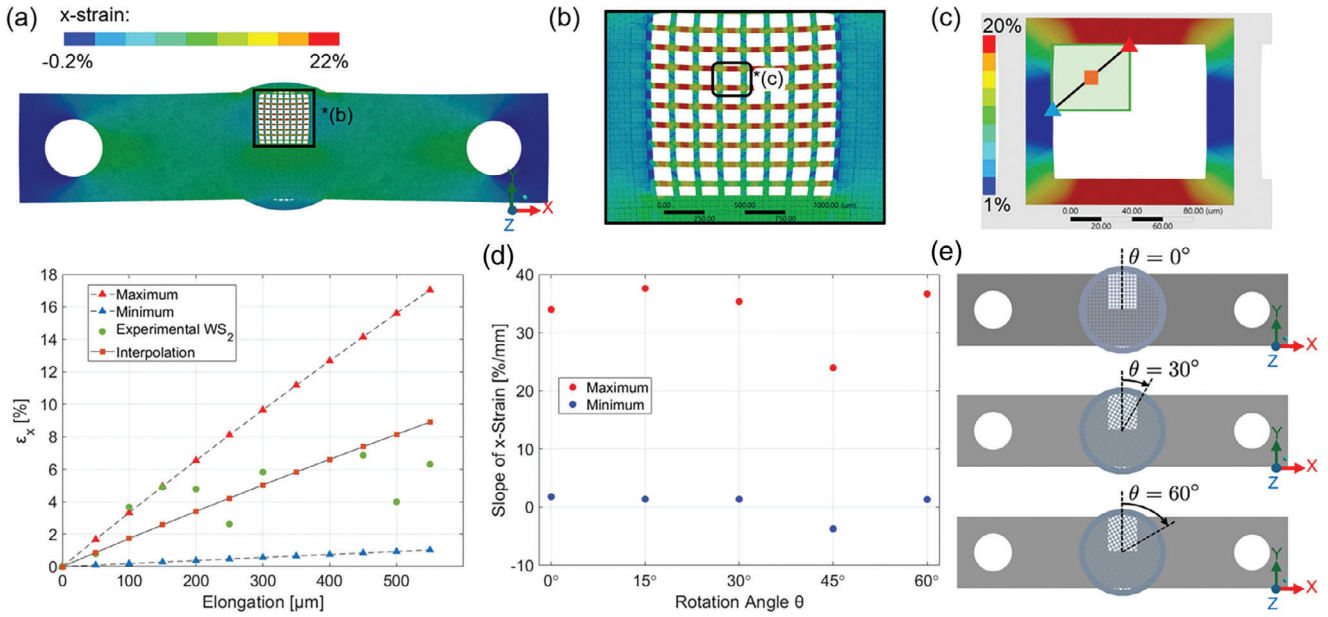

Figure 5. Tensile testing platform FEA simulations. a) Full *x*-strain (ε_x) contour plot of the copper sheet and TEM grid, with viewing window cut-out indicated. b) Magnified *x*-strain contour plot of the viewing window cut-out, with WS_2 imaging square indicated. c) Magnified *x*-strain contour plot of the WS_2 imaging square, with minimum, maximum, and interpolated strain nodes indicated (blue triangle, red triangle, and orange square, respectively). The approximate imaging region for WS_2 experiments is indicated by the green square. d) Plot of simulated true strain (*x*-strain) and experimental WS_2 crystal strain (*x*-strain) as a function of tensile testing platform elongation. e) Slope of simulated ε_x versus elongation for maximum and minimum strain nodes, plotted as a function of grid rotation angle θ. f) Schematic of 0°, 30°, and 60° grid rotation angles.

to estimate strains within the grid square itself (see Supporting Information). In Figure 5c, selected boundary nodes representing maximum and minimum strains (red and blue triangles, respectively) are indicated. Linear interpolation was used to find the true strain value at the orange square location between these two nodes. Based on low magnification survey images, the location of the WS_2 crystal is known to be somewhere within the area indicated by the green rectangle in Figure 5c.

Figure 5d plots the maximum true strain (red triangle location in Figure 5c), minimum true strain (blue triangle location in Figure 5c), and interpolated true strain (orange square location in Figure 5c) as a function of tensile testing platform elongation. The simulated true strains are compared with experimental values for WS_2 (green circles in Figure 5d) to validate the model. Overall, the results show good agreement between simulation and experiment, with experimental data points falling within the maximum and minimum bounds of simulated values for all elongations. Some deviation between experimental and interpolated values is observed, and may arise from a number of sources. First, the exact location of experimental imaging is unknown, and may have shifted with straining holder elongation. Second, model assumptions including linear elastic behavior of the copper grid bars and zero-slip conditions at all material interfaces (i.e., TEM grid-to-copper sheet, specimen-to-TEM grid) will introduce errors in the simulated values. At high elongations, the model tends to overpredict strain versus experiment. This suggests that the primary source of error is not the linear elastic assumption of the model or post-processing to account for the plastic regime, but more likely the occurrence of the specimen or adhesive slip during the experiment. We note that it is not possible to compare experimental and simulated values of strain for sputtered Au–Pd and electrodeposited Li experiments, as the imaging locations for these specimens are known with less precision than that of WS_2. Specimen strain is highly dependent on imaging location, as the results of Figure 5b clearly indicate. Additionally, the emergence of cracks or tears in the carbon support film, as seen in the Li thin films, significantly reduces the amount of strain experienced by the sample.

An additional factor to consider is the effect of grid rotation angle, θ, on specimen strain. It may at first appear surprising that experimental strains fall within the bounds of simulated strains in Figure 5d, when simulated values were obtained for 0° grid rotation and the experimental grid had some degree of rotation relative to the copper strip. To investigate the effect of grid rotation on specimen strains, FEA simulations were conducted for θ = 15°, 30°, 45°, and 60° (Figure 5f), and the slope of maximum and minimum engineering strain versus elongation curves plotted in Figure 5e. It should be noted that at $\theta = 0°$ the element size is 25 µm; at all other angles the element size is 15 µm to achieve a good mesh. From the plot, we can see that the tensile testing platform is robust to variations in grid rotation angles from 0–30°; however, at 45°, we see a more drastic change in the resulting specimen strain. The negative value in the minimum slope at 45° comes from two corners of the TEM grid coming closer together and causing a contraction of the grid bars (Figure S3, Supporting Information). At this grid rotation angle, in situ compression of the specimen is possible.

3. Conclusion

This work presents a facile approach for in situ TEM straining experiments and demonstrates its applicability toward three different methods of thin-film sample preparation. A simple uniaxial straining design combined with FEA simulation enables the tensile testing platform to achieve both simplicity of experimental methods and quantification of specimen strains. Experimental values of specimen strain determined from SAED patterns fall within the maximum and minimum bounds of strain predicted by FEA. The good agreement between simulation and experiment provides confidence that the tensile testing platform is successfully converting straining holder displacement into specimen strain. Additionally, the results validate the model's ability to quantify specimen strains and specimen strain non-uniformities across the viewing window. Non-uniformities in strain on a millimeter scale are important to account for when performing in situ straining experiments. This work demonstrates that these non-uniformities can be modeled by finite element simulations. Finally, the results presented here lay the groundwork for future in situ straining experiments on a wide variety of material classes, including those that have remained previously unexplored due to the challenges of in situ straining sample preparation. To emphasize ease of sample preparation, this demonstration of the tensile testing platform uses standard TEM grids as flexible substrates. We envision future work exploring alternate substrate designs that achieve more uniform strain distributions across the specimen. Additionally, the design of flexible substrates that stay within elastic deformation limits could provide opportunities for in situ cyclic loading of specimens.

4. Disclaimer

This document was prepared as an account of work sponsored by the United States Government. While this document is believed to contain correct information, neither the United States Government nor any agency thereof, nor the Regents of the University of California, nor any of their employees, makes any warranty, express or implied, or assumes any legal responsibility for the accuracy, completeness, or usefulness of any information, apparatus, product, or process disclosed, or represents that its use would not infringe privately owned rights. Reference herein to any specific commercial product, process, or service by its trade name, trademark, manufacturer, or otherwise, does not necessarily constitute or imply its endorsement, recommendation, or favoring by the United States Government or any agency thereof, or the Regents of the University of California. The views and opinions of authors expressed herein do not necessarily state or reflect those of the United States Government or any agency thereof or the Regents of the University of California.

5. Experimental Section

Preparation of Tensile Testing Platform: Commercially available copper foils of 25 µm thickness were machined into strips of size 11.5 mm × 2.5 mm. Two holes were drilled for clamping screws on either side of this platform and a slit was cut out, as shown in Figure S1a (Supporting Information). The slit width can be varied from 50 µm to as large as 2 mm depending on the requirements of the experiment. A conventional 3 mm TEM grid

with thin film specimen (Au–Pd, WS_2, or Li) was placed across this gap and affixed to the template using adhesive (Crystalbond or polyurethane epoxy).

TEM Sample Preparation: Au–Pd sputter-coated films were deposited on a grid using a Gatan Model 681 high-resolution ion beam coater operating at 9 keV beam energy and 300 µm current aimed at a target of Au–Pd alloy. Coating duration was 90 s, which yielded polycrystalline thin films of thickness ≈10 nm. Lacey formvar/carbon grids from Ted Pella (part number 01883) were used for this deposition.

Monolayer and few-layer WS_2 crystals were transferred to TEM grids using a polymer-assisted wet transfer process. WS_2 flakes were cleaved from a single crystal (SPI Supplies) onto a Si wafer with 285 nm SiO_2. Flakes were cleaved using Au-tape-assisted mechanical exfoliation.[44] In brief, a 100 nm gold film was deposited on a Si wafer, followed by spin coating with a layer of polyvinylpyrrolidone (PVP) polymer. A clean gold film was template-stripped from the Si substrate with thermal release tape, and was used to exfoliate a single crystal monolayer from bulk crystal. Subsequently, the PVP/gold/monolayer stack was released onto a SiO_2/Si substrate upon heating. The PVP layer was removed with water, and the gold layer was removed by gold etchant (KI/I_2) solution. Suitable WS_2 flakes were identified via optical inspection. The wafer was spin-coated at 2500 rpm with polystyrene dissolved in toluene and baked on a hot plate at 60 °C for 30 min. Immersion of this wafer into water led to detachment of the polystyrene film along with the WS_2 flakes. The detached polystyrene film with WS_2 flakes was scooped onto copper lacey formvar/carbon, 200 mesh grids (Ted Pella, part number 01883) and baked at 80 °C for 50 min to promote adhesion. TEM grids were placed in toluene to dissolve the remaining polystyrene. Details of this process are provided in other studies.[45–47]

Lithium specimens were prepared by direct electroplating of Li metal onto TEM grids, after the method of Zhai et al.[42] CR2032 coin cells were assembled in an Ar glovebox (< 0.1 ppm H_2O, < 0.1 ppm O_2). A lacey carbon, 200 mesh, copper grid (Electron Microscopy Sciences, LC200-CU) was placed directly onto the Cu current collector as the cell anode. Li metal foil on a stainless-steel disc was used as the cathode, with a Celgard 3501 separator and 1 M $LiPF_6$ in ethylene carbonate-dimethyl carbonate (1:1) electrolyte (60 µL). Cells were assembled using an MTI MSK-110 hydraulic crimper. Cells were allowed to rest for 24 h before electroplating, followed by open circuit voltage measurement for 30 min. Li plating was conducted using a cell current of 174 µA for 5 min using a Biologic VMP3 multichannel potentiostat (Figure S2, Supporting Information). Cells were disassembled in a glovebox immediately following electroplating. Grids were adhered to copper sheets in the glovebox using epoxy and stored under inert atmosphere until use.

TEM Data Collection and Analysis: In situ straining experiments of sputtered Au–Pd were conducted using a JEOL 3010 electron microscope operating at an accelerating voltage of 300 kV and equipped with a Gatan Orius 833 camera. In situ straining experiments of WS_2 were conducted using an FEI TitanX 60-300 electron microscope with a Gatan Orius 830 camera. In situ experiments of electrodeposited Li were conducted using an FEI ThemIS 60-300 microscope with a Gatan direct electron K2 camera. Copper strips containing the specimen were loaded onto a Gatan 654 single-tilt heating/straining holder. A constant elongation rate of 1 µm s^{-1} was applied during experiments, with TEM images and diffraction data recorded at different elongations. Beam acceleration voltage was reduced for WS_2 and electrodeposited Li specimens to minimize beam-induced sample damage.

Finite Element Analysis: Commercial CAD software SOLIDWORKS and SpaceClaim were used to create the surface geometries and assemble the tensile testing platform, respectively. TEM grid geometry (Figure S1b, Supporting Information) was based on a Gilder G200 grid, with exact dimensions obtained from the manufacturer's specification sheet. FEA simulations were performed using Ansys Mechanical. TEM grid bars and the copper sheet were treated as annealed copper with a Young's modulus of 110 GPa and a Poisson's ratio of 0.343. A shared topology contact was defined between the TEM grid bars and the copper sheet. The generated mesh for the TEM grid bars and copper sheet consisted of triangular elements. It was assumed that one end of the tensile testing platform remained perfectly rigid and perfectly clamped (zero displacement). The moving end of the tensile testing platform was confined to move in the *x*-direction, and the holes were assumed to remain rigid. The assumption that the holes remain rigid was justified because there is no interest in the strains at these locations. A verification calculation shows similar displacements if the hole is displaced using a bearing load boundary condition (Figure S4, Supporting Information). The solutions of interest from the FEA were the normal engineering strains (ε_x, ε_y) within the TEM grid area. A maximum displacement of 600 µm was applied to the copper sheet, with strain data recorded at increments of 50 µm. The TEM grid area within the viewing window cut-out was isolated for a mesh convergence study. The simulated engineering strains were then post-processed to true strain to account for the plastic regime (see Supporting Information).

Supporting Information

Supporting Information is available from the Wiley Online Library or from the author.

Acknowledgements

B.S. and M.D. contributed equally to this work. FEA simulations and in situ straining experiments of electrodeposited Li were supported in-part by National Science Foundation Award #2152562. Work at the Molecular Foundry was supported by the Office of Science, Office of Basic Energy Sciences, of the U.S. Department of Energy (DOE) under Contract No. DE-AC02-05CH11231 and Materials Sciences and Engineering Division under contract No.DE-AC02-05-CH11231 (EMAT program KC1201). WS_2 TEM sample fabrication and data analysis was supported by the US DOE Office of Science for support of microelectronics research, under contract number DE-AC02-05CH11231. The preparation of large area WS_2 monolayer materials is based upon work supported by the Defense Advanced Research Projects Agency (DARPA) under Agreement No. HR00112390108. A.C.J. acknowledges support from the DOE Office of Science Graduate Student Research (SCGSR) award and TomKat Center Graduate Fellowship for Translational Research. Straining experiments of electrodeposited lithium were also supported by the Assistant Secretary for Energy, Efficiency and Renewable Energy, Office of Vehicle Technologies of the U.S. Department of Energy under Contract No. DE-AC02-05CH11231. Laser cutting of the copper platforms was performed at the Advanced Light Source at LBNL, and in the lab of Prof. Peter Hosemann at UC Berkeley.

Conflict of Interest

The authors declare no conflict of interest.

Data Availability Statement

The data that support the findings of this study are available from the corresponding author upon reasonable request.

Keywords

2D materials, electron diffraction, finite element analysis, tensile testing, transmission electron microscopy

Received: September 16, 2024
Revised: December 5, 2024
Published online:

[1] J. Pelleg, *Mechanical Properties of Materials*, vol. *190*, Springer, Berlin **2013**.

[2] M. Meyers, O. Vöhringer, V. Lubarda, *Acta Mater.* **2001**, *49*, 4025.
[3] P. G. Callahan, J.-C. Stinville, E. R. Yao, M. P. Echlin, M. S. Titus, M. De Graef, D. S. Gianola, T. M. Pollock, *Ultramicroscopy* **2018**, *186*, 49.
[4] D. W. Pashley, *Proc. R. Soc. London A* **1960**, *255*, 218.
[5] U. Messerschmidt, F. Appel, *Ultramicroscopy* **1976**, *1*, 223.
[6] M. J. Hÿtch, A. M. Minor, *MRS Bull.* **2014**, *39*, 138.
[7] X. Li, M. Sun, C. Shan, Q. Chen, X. Wei, *Adv. Mater. Interfaces* **2018**, *5*, 1701246.
[8] Y. Han, L. Wang, K. Cao, J. Zhou, Y. Zhu, Y. Hou, Y. Lu, *Chem. Rev.* **2023**, *123*, 14119.
[9] M. Haque, M. Saif, *Int. J. Mater. Res.* **2005**, *20*, 1769.
[10] A. M. Beese, D. Papkov, S. Li, Y. Dzenis, H. D. Espinosa, *Carbon* **2013**, *60*, 246.
[11] D. Zhang, J.-M. Breguet, R. Clavel, L. Philippe, I. Utke, J. Michler, *Nanotechnology* **2009**, *20*, 365706.
[12] S. Manchuraju, A. Kroeger, C. Somsen, A. Dlouhy, G. Eggeler, P. Sarosi, P. Anderson, M. Mills, *Acta Mater.* **2012**, *60*, 2770.
[13] B. G. Demczyk, Y. M. Wang, J. Cumings, M. Hetman, W. Han, A. Zettl, R. Ritchie, *Mater. Sci. Eng., A* **2002**, *334*, 173.
[14] K. Cao, S. Feng, Y. Han, L. Gao, T. Hue Ly, Z. Xu, Y. Lu, *Nat. Commun.* **2020**, *11*, 284.
[15] D. Kiener, A. M. Minor, *Nano Lett.* **2011**, *11*, 3816.
[16] H. Idrissi, C. Bollinger, F. Boioli, D. Schryvers, P. Cordier, *Sci. Adv.* **2016**, *2*, 1501671.
[17] A. Bo, K. Chen, E. Pickering, H. Zhan, J. Bell, A. Du, Y. Zhang, X. Wang, H. Zhu, Z. Shan, Y. Gu, *J. Phys. Chem. Lett.* **2018**, *9*, 6052.
[18] K. Sato, H. Miyazaki, T. Gondo, S. Miyazaki, M. Murayama, S. Hata, *Microscopy* **2015**, *64*, 369.
[19] T. Higuchi, T. Gondo, H. Miyazaki, A. Kumagai, K. Akutagawa, H. Jinnai, *Microscopy* **2018**, *67*, 296.
[20] T. Miyata, H.-F. Wang, D. Watanabe, Y. Kawagoe, T. Okabe, H. Jinnai, *Microscopy* **2023**, *73*, 208.
[21] D. Gong, M. Zhu, Z. You, H. Han, Z. Chao, L. Jiang, *Composites, Part B* **2022**, *244*, 110180.
[22] J. Liu, C. Chen, Q. Feng, X. Fang, H. Wang, F. Liu, J. Lu, D. Raabe, *Mater. Sci. Eng., A* **2017**, *703*, 236.
[23] T. C. Pekin, C. Gammer, J. Ciston, C. Ophus, A. M. Minor, *Scr. Mater.* **2018**, *146*, 87.
[24] Y. Chen, Y. Fang, X. Fu, Y. Lu, S. Chen, H. Bei, Q. Yu, *J. Mater. Sci. Technol.* **2021**, *73*, 101.
[25] Y. Bu, Z. Li, J. Liu, H. Wang, D. Raabe, W. Yang, *Phys. Rev. Lett.* **2019**, *122*, 075502.
[26] Y. Xiang, T. Li, Z. Suo, J. J. Vlassak, *Appl. Phys. Lett.* **2005**, *87*, 16.
[27] O. Akogwu, D. Kwabi, S. Midturi, M. Eleruja, B. Babatope, W. Soboyejo, *Mater. Sci. Eng., B* **2010**, *170*, 32.
[28] R. Roldán, A. Castellanos-Gomez, E. Cappelluti, F. Guinea, *J. Phys.: Condens. Matter* **2015**, *27*, 313201.
[29] I. Niehues, A. Blob, T. Stiehm, S. M. de Vasconcellos, R. Bratschitsch, *Nanoscale* **2019**, *11*, 12788.
[30] T. Li, Z. Huang, Z. Xi, S. P. Lacour, S. Wagner, Z. Suo, *Mech. Mater.* **2005**, *37*, 261.
[31] N. Lu, X. Wang, Z. Suo, J. Vlassak, *Appl. Phys. Lett.* **2007**, *91*, 22.
[32] M. Schwartzkopf, A. Buffet, V. Körstgens, E. Metwalli, K. Schlage, G. Benecke, J. Perlich, M. Rawolle, A. Rothkirch, B. Heidmann, G. Herzog, P. Müller-Buschbaum, R. Röhlsberger, R. Gehrke, N. Stribeckb, S. V. Roth, *Nanoscale* **2013**, *5*, 5053.
[33] S. Jeon, T. Heo, S.-Y. Hwang, J. Ciston, K. C. Bustillo, B. W. Reed, J. Ham, S. Kang, S. Kim, J. Lim, K. Lim, J. S. Kim, M.-H. Kang, R. S. Bloom, S. Hong, K. Kim, A. Zettl, W. Y. Kim, P. Ercius, J. Park, W. C. Lee, *Science* **2021**, *371*, 498.
[34] B. H. Savitzky, S. E. Zeltmann, L. A. Hughes, H. G. Brown, S. Zhao, P. M. Pelz, T. C. Pekin, E. S. Barnard, J. Donohue, L. R. DaCosta, E. Kennedy, Y. Xie, M. T. Janish, M. M. Schneider, P. Herring, C. Gopal, A. Anapolsky, R. Dhall, K. C. Bustillo, P. Ercius, M. C. Scott, J. Ciston, A. M. Minor, C. Ophus, *Microsc. Microanal.* **2021**, *27*, 712.
[35] J.-L. Rouviere, A. Béché, Y. Martin, T. Denneulin, D. Cooper, *Appl. Phys. Lett.* **2013**, *103*, 24.
[36] D. Cooper, T. Denneulin, N. Bernier, A. Béché, J.-L. Rouvière, *Micron* **2016**, *80*, 145.
[37] Y. Han, L. Gao, J. Zhou, Y. Hou, Y. Jia, K. Cao, K. Duan, Y. Lu, *ACS Appl. Mater. Interfaces* **2022**, *14*, 8655.
[38] H. J. Conley, B. Wang, J. I. Ziegler, R. F. Haglund Jr, S. T. Pantelides, K. I. Bolotin, *Nano Lett.* **2013**, *13*, 3626.
[39] M. J. Hamer, D. G. Hopkinson, N. Clark, M. Zhou, W. Wang, Y. Zou, D. J. Kelly, T. H. Bointon, S. J. Haigh, R. V. Gorbachev, *Nano Lett.* **2020**, *20*, 6582.
[40] F. Carrascoso, H. Li, J. M. Obrero-Perez, F. J. Aparicio, A. Borras, J. O. Island, A. Barranco, A. Castellanos-Gomez, *npj 2D Mater. Appl.* **2023**, *7*, 24.
[41] J. Z. Lee, T. A. Wynn, M. A. Schroeder, J. Alvarado, X. Wang, K. Xu, Y. S. Meng, *ACS Energy Lett.* **2019**, *4*, 489.
[42] W. Zhai, B. Yuan, Y. Fan, Y. Zhang, X. Zhang, Y. Ma, W. Liu, Y. Yu, *J. Am. Chem. Soc.* **2022**, *144*, 4124.
[43] Y. Xu, H. Wu, H. Jia, J.-G. Zhang, W. Xu, C. Wang, *ACS Nano* **2020**, *14*, 8766.
[44] F. Liu, W. Wu, Y. Bai, S. H. Chae, Q. Li, J. Wang, J. Hone, X.-Y. Zhu, *Science* **2020**, *367*, 903.
[45] S. Chen, H. Liu, F. Chen, K. Zhou, Y. Xue, *ACS Nano* **2020**, *14*, 11473.
[46] A. J. Watson, W. Lu, M. H. Guimar aes, M. Stöhr, *2D Mater.* **2021**, *8*, 032001.
[47] A. Gurarslan, Y. Yu, L. Su, Y. Yu, F. Suarez, S. Yao, Y. Zhu, M. Ozturk, Y. Zhang, L. Cao, *ACS Nano* **2014**, *8*, 11522.